

The 2014 March 29 X-flare: sub-arcsecond resolution observations of Fe XXI $\lambda 1354.1$

Peter R. Young

College of Science, George Mason University, Fairfax, VA 22030, USA

Hui Tian

Harvard-Smithsonian Center for Astrophysics, 60 Garden Street, Cambridge, MA 02138, USA

Sarah Jaeggli

Department of Physics, Montana State University, P.O. Box 173840, Bozeman, MT 59717, USA

ABSTRACT

The Interface Region Imaging Spectrometer (IRIS) is the first solar instrument to observe ~ 10 MK plasma at subarcsecond spatial resolution through imaging spectroscopy of the Fe XXI $\lambda 1354.1$ forbidden line. IRIS observations of the X1 class flare that occurred on 2014 March 29 at 17:48 UT reveal Fe XXI emission from both the flare ribbons and the post-flare loop arcade. Fe XXI appears at the ribbon locations around 75 seconds after the ribbons appear in the chromospheric continuum, and $\lambda 1354.1$ shows blue-shifts of $100\text{--}200$ km s $^{-1}$, suggesting hot plasma upflow into the corona. The Fe XXI ribbon emission is compact with a spatial extent of $< 2''$, and can extend beyond the chromospheric ribbon locations. Examples are found of both decreasing and increasing blue-shift in the direction away from the ribbon locations, and blue-shifts were present for at least 6 minutes after the flare peak. The post-flare loop arcade, seen in Atmospheric Imaging Assembly (AIA) 131 Å filtergram images that are dominated by Fe XXI, exhibited bright loop-tops with an asymmetric intensity distribution. The sizes of the loop-tops are resolved by IRIS at $\geq 1''$, and line widths in the loop-tops are not broader than in the loop-legs suggesting the loop-tops are not sites of enhanced turbulence. Line-of-sight speeds in the loop arcade are typically < 10 km s $^{-1}$, and mean non-thermal motions fall from 43 km s $^{-1}$ at the flare peak to 26 km s $^{-1}$ six minutes later. If the average velocity in the loop arcade is assumed to be at rest, then it implies a new reference wavelength for the Fe XXI line of 1354.106 ± 0.023 Å.

Subject headings: Sun: flares — Sun: activity — Sun: corona — Sun: UV radiation — Sun: chromosphere

1. Introduction

The 3P_0 – 3P_1 ground transition of Fe XXI gives rise to an emission line at 1354.1 Å that was first identified from *Skylab* S082B spectra by Doschek et al. (1975). It is the strongest emission line formed at temperatures ≥ 10 MK that is found longward of the hydrogen Lyman limit, and it is of great interest for studying plasma dynamics during flares on account of the much higher spectral resolution possible at ultraviolet wavelengths compared to X-ray wavelengths. The first observations of Doschek et al. (1975) demonstrated for one flare that the line width decreased as the flare evolved, and Doppler motions did not exceed 20 km s^{−1}. Cheng et al. (1979) studied 17 *Skylab* flares and used $\lambda 1354.1$ to determine non-thermal velocities ranging between 0 and 60 km s^{−1}. Note that the S082B instrument had a 2'' × 60'' slit but no spatial resolution along the slit, thus the spatial resolution of the instrument depended on the spatial extent of the observed flare.

Mason et al. (1986) analyzed seven flares observed with the Ultraviolet Spectrometer and Polarimeter (UVSP) on board the Solar Maximum Mission (SMM), and found examples of asymmetries in the line profile during the rise phase of flares that indicated plasma upflowing at speeds of up to 200 km s^{−1}. Smaller asymmetries were also found during the soft X-ray peaks of the flares, suggesting evaporation was continuing at this stage of the flare. The spatial resolution of UVSP was determined by the size of the entrance slit used, which could be as small as 3'' × 3''.

The Solar Ultraviolet Measurement of Emitted Radiation (SUMER) instrument on board the Solar and Heliospheric Observatory (SOHO) observed the Fe XXI line, but only in off-limb flares. A M7.6 flare on 1999 May 9 was captured with a full spectrum scan by SUMER and studied by Feldman et al. (2000), Innes et al. (2001) and Landi et al. (2003). The Fe XXI line was observed about 3 hours after the flare peak, and Feldman et al. (2000) derived a new rest wavelength of 1354.064 ± 0.020 Å for the line, and Landi et al. (2003) found non-thermal broadening in the line corresponding to 30–40 km s^{−1}. Fe XXI $\lambda 1354.1$ was also recorded in the X-class flare of 2002 April 21, which produced a supra-arcade of hot plasma that displayed dynamic, dark voids (Innes et al. 2003a,b). Blueshifts of up to 1000 km s^{−1} were seen in this data-set, and $\lambda 1354.1$ was used to constrain the temperature of the dark voids. A further use of $\lambda 1354.1$ from SUMER data was to study Doppler shift oscillations in hot active region loops (Kliem et al. 2002; Wang et al. 2003a), which are triggered by microflares and are interpreted as standing slow-mode magnetoacoustic waves (Wang et al. 2003b).

The Fe XXI line was first reported in a non-solar spectrum by Maran et al. (1994) who measured the line in a Goddard High Resolution Spectrometer spectrum of the star AU Microscopii. A survey of measurements of the line in cool stars was presented by Ayres et al. (2003) based on Space Telescope Imaging Spectrograph (STIS) data.

Fe XXI is only expected to be found in the solar spectrum during flares and there are two key spatial locations expected from the standard model of solar flares. The standard model (see the review of Benz 2008) specifies an energy release site in the corona, usually assumed to be the location of magnetic reconnection. Energy from the release site is transmitted down the legs of

coronal loops in the form of non-thermal particles, a thermal conduction front, or Alfvén waves. The energy is deposited in the dense chromosphere, leading to plasma heating, and the subsequent expansion of the plasma results in the “evaporation” of hot plasma into the coronal loops. Fe XXI is formed at ≈ 10 MK, and we expect to find 10 MK plasma concentrated at the loop footpoints due to the initial chromospheric heating, followed later by the appearance of bright 10 MK loops that are formed from the evaporated plasma. A key prediction of the standard flare model is that the plasma at the footpoints will flow upwards into the loops as the evaporation process proceeds and thus blue-shifted emission lines are expected. Spatially-resolved spectral data from the Coronal Diagnostic Spectrometer (CDS) on board SOHO, and the EUV Imaging Spectrometer (EIS) on board the Hinode spacecraft have demonstrated that blue-shifted emission is seen in emission lines of Fe XIX, Fe XXIII and Fe XXIV and speeds can be as high as 400 km s^{-1} (Teriaca et al. 2003, 2006; Milligan et al. 2006; Watanabe et al. 2011; Young et al. 2013). The flare loop footpoints are expected to coincide with the flare ribbons that are seen in $H\alpha$ and UV continuum images, although this can not be directly confirmed with CDS and EIS, which observe extreme ultraviolet radiation.

The Interface Region Imaging Spectrometer (IRIS) was launched in 2013 July and it observes the 1332–1358 Å wavelength region at a spatial resolution of $0.33\text{--}0.40''$, significantly better than the previous instruments that have observed the Fe XXI line. The high spatial resolution enables the fine-scale structure of the Fe XXI line to be investigated, particularly with regard flare loops and their footpoints. We present observations obtained by IRIS of the X1 class flare that occurred on 2014 March 29, peaking at 17:48 UT (SOL2014-03-29T17:48), and the paper is structured as follows. Sect. 2 gives an overview of the March 29 flare observation and describes the data-sets. Sect. 3 defines flares ribbons and kernels in the context of the IRIS data, and Sect. 4 describes how the Fe XXI emission in the vicinity of the ribbons behaves. Sect. 5 discusses properties of the post-flare loop arcade, and Sect. 6 summarizes the results.

2. Observations

The flare occurred in active region AR 12017 which was part of a larger complex that included AR 12018. The 1–8 Å GOES light curve is plotted in Figure 1 and shows that the flare began at 17:35 UT with an initial rise from a GOES class level B9 to C3 by 17:41 UT. A rapid rise to the X1 level began at 17:44 UT, with the peak reached at 17:48 UT.

IRIS is described in detail by De Pontieu et al. (2014) and is briefly summarized here. The instrument returns narrow-slit spectral data over three wavelength bands of 1332–1358, 1389–1406 and 2782–2834 Å, and a slit-jaw imager can produce images centered at 1330, 1400, 2796 and 2832 Å, giving context images for the spectra. The spectrometer slit is $0.33''$ wide, and the detector pixel sizes correspond to $0.167''$. The strongest emission lines observed by the instrument are Mg II $\lambda\lambda 2796.4, 2803.5$, C II $\lambda\lambda 1334.5, 1335.7$, and Si IV $\lambda\lambda 1393.8, 1402.8$, which are formed in the chromosphere and transition region. Fe XXI $\lambda 1354.1$ is the only coronal line in the present data-set that can yield sufficient signal-to-noise for detailed studies of line profiles.

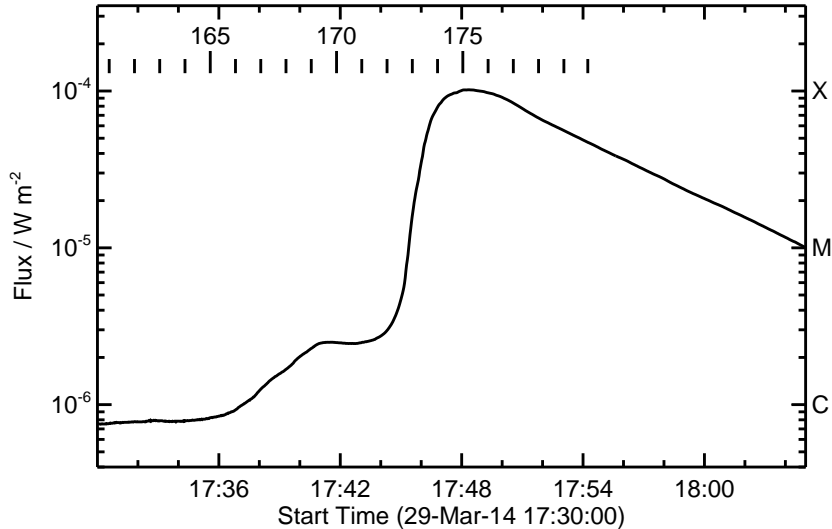


Fig. 1.— The GOES 1–8 Å light curve for the period 17:30–18:05 UT on 2014 March 29. Short vertical lines indicate the start and end times of the IRIS rasters, and the IRIS raster numbers are indicated.

For the present flare observation IRIS performed 180 raster scans over the period 14:09 to 17:54 UT. Each scan consisted of eight slit positions separated by $2''$, giving a total raster size of $14.33''$. The field-of-view in the solar-Y direction was $175''$ and 8 second exposures were used. The duration of each raster was 75 seconds. A slitjaw image was obtained with each raster exposure: four were obtained at 2796 \AA with each raster, three at 1400 \AA , and one at 2832 \AA . Saturation on the detector was a problem for the strong IRIS lines during the flare (particularly $\text{Si IV } \lambda 1402$), but $\text{Fe XXI } \lambda 1354.1$ was not saturated at any location. We focus on rasters 171–179, which cover the rise and initial-decay phases of the flare (Figure 1). We note that there was weak Fe XXI from the active region prior to this time period that is related to the weaker C3 event, but our focus in the present work is on the flare ribbons and post-flare loops of the X1 event. As a shorthand in the present work we will refer to specific IRIS exposures as, e.g., R174E0, which refers to raster no. 174 and exposure no. 0. The raster numbers go from 0 to 179 and the exposure numbers from 0 to 7 (note that IRIS rasters from east to west). When giving times for these exposures, we give the mid-time of the exposure.

Level-2 IRIS data were downloaded from the IRIS website and they are corrected for most instrumental effects, including geometric distortions, flat-fields and spatial alignments. The version of the calibration processing routine (IRIS_PREP) applied to the data was 1.27. Intensities are given in data-number (DN) units and $1\text{-}\sigma$ uncertainties are derived as follows. An intensity of d DN corresponds to p photons, given by:

$$p = 2.94 \times 10^{-4} g \lambda d = kd \tag{1}$$

where g is the CCD gain, which takes a value of 6 for the IRIS far-ultraviolet (FUV) channel (De Pontieu et al. 2014), λ is the wavelength in Å, and $2.94 \times 10^{-4} \text{ Å}^{-1}$ is the energy required to produce an electron-hole pair in silicon. Assuming Poisson noise, the uncertainty on p is \sqrt{p} , however the dark current uncertainty, σ_{dc} , also needs to be included, giving

$$\sigma_p = \sqrt{p + (k\sigma_{\text{dc}})^2} \quad (2)$$

De Pontieu et al. (2014) give a value of $\sigma_{\text{dc}} = 3.1$ DN for the FUV channel. Defining the fractional error to be $f = \sigma_p/p$, the uncertainty on d is then $\sigma_d = fd$. This method for computing the intensity uncertainties is implemented in the *Solarsoft* IDL routine IRIS_GETWINDATA.

We found that the best way to study the $\lambda 1354.1$ emission line for this data-set was through exposure images (wavelength vs. solar-Y) as they allow the difference in morphology between the broad $\lambda 1354.1$ line and the narrow blending cool lines to be more easily discerned. The raster is too sparse for X-Y images to accurately reflect the intensity distribution across the raster and for this it is better to consider 131 Å images from the Atmospheric Imaging Assembly on board the Solar Dynamics Observatory.

The AIA instrument is described in Lemen et al. (2012), and the images considered in the present work are from the 131 Å filter (hereafter referred to as “A131”), which is dominated by Fe XXI $\lambda 128.75$ during flares and thus is ideal for comparisons with the IRIS slit images. Additional contributing lines are Fe XX $\lambda 132.84$ and Fe XXIII $\lambda 132.91$. The image spatial scale is $0.6''$ per pixel, and the cadence is 12 seconds. An automatic observing procedure is initiated during flares when count rates become large. Every alternate frame remains at the nominal exposure time, with the exposure times for the remaining frames adjusted through an automatic exposure control mechanism. Despite this, the rapid intensity increases during the flare still led to many frames that were badly affected by saturation. In the present case from 17:46 UT to the end of the IRIS sequence at 17:54:19 UT there are only 12 A131 exposures for which saturation is sufficiently low to allow comparison with the IRIS data, however these images still yield valuable comparisons with the IRIS data as demonstrated in the following sections.

The wavelength of Fe XXI $\lambda 1354.1$ was given as $1354.08 \pm 0.05 \text{ Å}$ by Sandlin et al. (1977) based on *Skylab* S082B measurements, and Feldman et al. (2000) gave a value of $1354.064 \pm 0.020 \text{ Å}$ from SUMER spectra. In the present article we derive a new value for the reference wavelength of $1354.106 \pm 0.023 \text{ Å}$ (Appendix B). The temperature of maximum emission of $\lambda 1354.1$ is $\log T/\text{K} = 7.06$, as obtained from atomic data in version 7.1 of the CHIANTI database (Dere et al. 1997; Landi et al. 2013). This temperature translates to a full-width at half-maximum (FWHM) emission line width of 0.438 Å , or 96.9 km s^{-1} in velocity space. The instrumental width is 25.85 mÅ (De Pontieu et al. 2014) and so is essentially negligible when studying $\lambda 1354.1$ line width measurements.

3. Flare ribbons

As stated in the Introduction, energy from the coronal energy release site of a flare travels to the chromosphere down coronal loop legs, leading to heating which is revealed through bright flare ribbons seen in $H\alpha$ and UV continuum images. We expect to see Fe XXI emission at these ribbons due to the rapid heating that occurs there. In this section we discuss properties of flare ribbons and their appearance in IRIS data.

Flare ribbons are a characteristic feature of $H\alpha$ flare observations and appear as narrow, curved, bright lines across the solar surface. Pairs of ribbons are common, but they can have complex shapes and discontinuities. The ribbons resolve into lines of compact kernels, and the sizes of the kernels have been measured to 0.6–1.9'' in one case, with smaller sizes corresponding to deeper atmospheric depths (Xu et al. 2012). Flare kernels can be seen in white light flares, but are much more easily seen in the UV continuum, such as the 1700 Å channel of the Transition and Coronal Explorer (TRACE, Handy et al. 1999) and AIA. Young et al. (2013) reported an AIA measurement of a flare kernel and found that it emitted in all of the the EUV channels of AIA, with a size at the resolution of the instrument ($\approx 1.2''$).

The IRIS instrument observes at FUV and near-ultraviolet (NUV) wavelengths, and the ribbons can be measured in both the continuum and the emission lines. The FUV continuum enhancement during flares is believed to be driven by backwarming from C II $\lambda\lambda 1334, 1335$ and Si IV $\lambda\lambda 1393, 1402$ (Doyle & Phillips 1992). We thus expect the FUV continuum ribbons to be correlated with the brightness of these emission lines (which are measured by IRIS). Although beyond the scope of the present work, we note that inspection of the March 29 flare suggests that this is indeed the case.

We are interested in the location of Fe XXI emission relative to the ribbons, and so we define ribbons to be the locations where the continuum is enhanced. Typically the ribbons are bright over regions of $\leq 1''$, but more complex structure is also seen where the continuum is enhanced over a broad region of a few arcseconds in size, with a brighter, $\leq 1''$ region embedded within it.

The Si IV $\lambda 1402$ line is badly saturated at the locations of the ribbons in the IRIS spectral data, but Figure 2 shows an example image from the 1400 Å slitjaw image during the flare rise phase where the ribbons are clearly seen. We highlight the features labeled N1, N2 and S1 in this figure, which are the ribbons for which IRIS spectra are available. The image is saturated in the N1 and especially the S1 ribbons, but in the weaker intensity areas it is clear that the ribbon emission contains numerous kernels, some as small as the instrument resolution (0.3'').

4. Fe XXI at the ribbons

We consider Fe XXI emission at the flare ribbon sites separately from the emission coming from the post-flare loop arcade, which is considered in the following section. The distinction is primarily

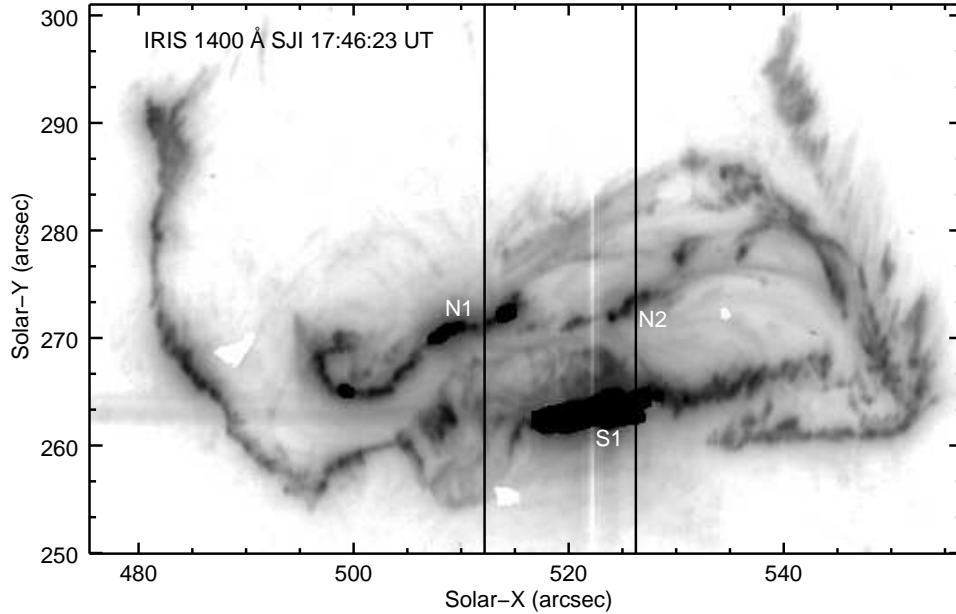


Fig. 2.— An IRIS 1400 Å slitjaw image from 17:46:23 UT, with a reverse-logarithmic intensity scaling applied. The locations of three flare ribbons are indicated by N1, N2 and S1 (N, S for north, south). The N1 and S1 ribbons are partially saturated. The two vertical lines show the limits of the IRIS raster.

in the Doppler velocity of the emission line, which is mostly blue-shifted at the ribbons whereas in the loops the line-of-sight (LOS) velocity is close to zero. As discussed in the Introduction, blue-shifted emission from highly-ionized iron lines has been studied previously with the CDS and EIS instruments. The key advances with IRIS are the much higher spatial resolution of the instrument, and simultaneous, co-spatial observations of the UV continuum and chromospheric emission lines, giving a direct link to the low atmosphere ribbon emission. Note that, as discussed in the previous section, the flare ribbons are defined here to be those spatial locations where the far-ultraviolet continuum observed by IRIS is enhanced.

The contrast between the broad Fe XXI line and the surrounding, narrow chromospheric lines makes it advantageous to study the detector images of the lines, which display intensity in the wavelength and solar-Y dimensions. In Figure 3 we show three consecutive detector images from IRIS raster exposure 0 alongside A131 images that are close in time. The parallel white lines on these images indicate the position of the IRIS slit. The R172E0 exposure shows the initial appearance of the ribbon, with a narrow, $\approx 0.3''$ extent in the Y-direction in terms of continuum emission, and a slightly larger extent in the chromospheric lines. There is no Fe XXI emission in this exposure. The R173E0 exposure, 75 seconds later, shows more intense ribbon emission in the continuum and chromospheric lines, and weak Fe XXI emission concentrated at the ribbon at a velocity of $\approx -100 \text{ km s}^{-1}$. Figure 4a shows a 1D cut through this image at $Y=270.0''$, offset $0.33''$

to the south of the ribbon to better show the Fe XXI line. It is seen as a broad feature between -190 and -30 km s^{-1} , although significantly blended with narrow chromospheric lines, as discussed later. The two A131 images corresponding to the first two IRIS exposures probably do not contain any significant emission from Fe XXI. Instead the emission is likely dominated by Fe VIII at 0.8 MK, although we note that the second A131 image was obtained 42 seconds prior to the IRIS exposure due to extensive saturation in the later images. The third IRIS exposure shows stronger Fe XXI emission from the ribbon, and also weak emission coming from the post-flare loop arcade – seen as two broad emission patches at $Y=266''$ and $270''$. The A131 image shows hook-shaped ribbon emission between $X=495$ to $515''$ and $Y=265$ to $277''$ (compare with the ribbons in Figure 2) and the IRIS slit passed through a kernel at $Y=273''$. Strong Fe XXI emission dominates the A131 image at the location (512,267).

Figures 3 and 4a demonstrate that a number of chromospheric lines become strong at the ribbon location, compromising studies of the Fe XXI line. The examples from the March 29 flare show that the blending lines are always present at the ribbons, although they are stronger for the S1 ribbon compared to the N1 and N2 ribbons. A further complication is that some of the lines, particularly, Si II $\lambda 1352.64$ and $\lambda 1353.72$ (at velocities -325 and -85 km s^{-1} relative to $\lambda 1354.1$), can exhibit significant broadening and Doppler shifts in some locations. Further examples of ribbon spectra are shown in Figure 4, and a discussion of the blending lines is given in Appendix A.

Figure 3 shows the development of Fe XXI at one location on the N1 ribbon (Figure 2), and in total we identify 14 distinct ribbon locations observed by IRIS: exposures 0 and 1 of the IRIS raster observe ribbon N1; exposures 1 to 7 observe ribbon S1; and exposures 3 to 7 observe the N2 ribbon. Fe XXI emission is seen at or just offset from the ribbon in all 14 cases, and Table 1 presents properties for each of the ribbon locations based on a visual inspection of the IRIS detector images. For each ribbon location we note the raster number in which the ribbon appeared, and the raster number in which Fe XXI emission at or close to the ribbon appeared. For eight of the ribbon locations, Fe XXI appeared after one raster (75 seconds later), for three exposures it appeared at the same time as the ribbon, and for the remaining three it appeared after two rasters (150 seconds later).

The morphology of Fe XXI ribbon emission in the detector images varies and is classified in Table 1 according to “position” and “type”, which we illustrate in Figure 5 where example detector images from the N1 and N2 ribbons (Figures 5a,b) and the S1 ribbon (5c,d) are shown. Position indicates whether $\lambda 1354.1$ is seen directly at the ribbon location (“ribbon”), or offset in Y from it (“offset”). Examples of the former are shown in Figures 5a and b where the ribbons are at $Y=272.5''$ and the Fe XXI line is clearly present. Examples of offset emission are shown in Figure 5c and d, where Fe XXI can not be identified directly at the ribbon sites, but it can be seen slightly offset ($< 1''$) from them. (Note that this offset emission is distinct from post-flare loop emission which is found several arcseconds from the ribbon locations in both Figures 5c and d.) This may indicate that the hot plasma is not found at exactly the same location as the low atmosphere ribbon. Type indicates whether the emission is compact ($< 1''$) in the Y-direction, whether it is extended

($\geq 1''$), and whether it has a “diagonal-in” or “diagonal-out” shape. The latter terms refer to the morphology of the Fe XXI emission in the detector images; whether it extends diagonally inwards towards the rest wavelength of the Fe XXI, or whether it extends diagonally outwards away from the rest wavelength. Figures 5a,d show examples of “compact” emission, Figure 5b an example of “diagonal-in”, and Figure 5c an example of “diagonal-out”. From the standard flare model we may expect to see the “diagonal-in” type, whereby strong blueshifts are found at the flare ribbon where evaporation is initiated; the magnitude of the blueshift would then decrease away from the ribbon as the upflowing plasma is decelerated as it rises up the coronal loop (perhaps encountering pre-existing plasma in the loop). The compact type may be explained through viewing geometry if the loop is inclined to the IRIS slit: the footpoint on the flare ribbon is observed by IRIS, but the loop leg is not aligned to the IRIS slit and so is not observed. This may also explain why the Fe XXI emission in Figure 5b is abruptly terminated at $Y=272.1''$. The “diagonal-out” type is unexpected and may indicate that plasma continues to be accelerated away from the ribbon site at this location.

The velocities of Fe XXI $\lambda 1354.1$ at the ribbons are generally quite low, with values typically around -100 km s^{-1} (column 6 of Table 1 and Figures 4a,b and d), significantly smaller than the velocities of $\approx -400 \text{ km s}^{-1}$ found by Watanabe et al. (2011) and Young et al. (2013) from the Fe XXIII and Fe XXIV lines observed by EIS for two flares. This may be due to lower velocities at the cooler temperature of Fe XXI and a less favorable line-of-sight, although we also note that the IRIS data window used for the observation did not extend beyond -350 km s^{-1} from the line center, thus very large velocities $\leq -400 \text{ km s}^{-1}$ could not be detected. The largest blueshift seen in the IRIS data was from the S1 ribbon observed in R174E5 (Figure 5c) for which the centroid reached $\approx -250 \text{ km s}^{-1}$ (Figure 4c). The profile was also very broad and apparently asymmetric. An asymmetric profile can also be identified from exposure R174E7 (Figure 4d). The blending lines complicate interpretation of the $\lambda 1354.1$ line widths, but the profiles shown in Figure 4 have FWHMs at least as wide as the thermal width (96.9 km s^{-1}), and significantly larger in the case of Figure 4c.

Another contrasting feature with the profiles presented by Watanabe et al. (2011) and Young et al. (2013) is the lack of a two-component structure to the Fe XXI line, in particular the absence of a component near the rest wavelength. This may suggest that the EIS observations did not resolve the upflowing flare kernel sites from the stationary flare loop plasma, although Young et al. (2013) were able to demonstrate that the flare kernel they studied was isolated in co-temporal AIA images. Careful alignment of IRIS and EIS data is needed to determine whether the stationary component is missing from the Fe XXI line or whether it is simply due to a blending of loop and footpoint emission in the EIS data.

The IRIS observations terminate at 17:54:19 UT, only 6 minutes after the flare peak, and blue-shifted Fe XXI is still present at this time as demonstrated in Figure 6, which shows the final IRIS exposure from the sequence. The ribbon is apparently broad at this stage as the continuum extends over $3''$, from $Y=258$ to $261''$, although we highlight the fact that C I $\lambda 1354.29$ has an

enhanced long-wavelength wing only at $Y=258''$, which may indicate a distinct structure within the ribbon. It can be seen that the upflow speed remains at around -100 km s^{-1} , similar to the values found when the Fe XXI emission initially appears during the flare rise phase (Table 1). By comparing the A131 image with the IRIS exposure we can clearly see the post-flare loop arcade and the transition from weak, blue-shifted footpoint emission to strong, stationary plasma within the loops.

To summarize, Fe XXI $\lambda 1354.1$ is not easy to measure at the flare ribbons on account of the intrinsically weak emission and the presence of a number of cool emission lines, some of which are broadened and/or demonstrate enhanced short wavelength wings at the ribbon site. However, the IRIS data show that Fe XXI is seen at or very close to all of the ribbon locations, typically about 75 seconds after the ribbons appear. Blueshifts typically correspond to velocities of -100 to -200 km s^{-1} , and the spatial extent (in solar- Y) of the Fe XXI ribbon emission is about $1''$. A single emission line component is always seen at the ribbons and the widths are at least as large as the thermal width of the line. Blue-shifted Fe XXI emission at the ribbon locations is clearly seen until the end of the IRIS sequence at 17:54 UT, six minutes after the flare peak.

5. Fe XXI in the flare loops

Fe XXI emission from the post-flare loop arcade began to dominate at 17:47 UT and Figure 7 shows three A131 images obtained between 17:48 and 17:53 UT. A striking feature of these images, particularly at 17:53:00 UT, is that the loops had bright knots of emission towards the loop apexes. This feature of post-flare loops has been reported previously from *Yohkoh* X-Ray Telescope data (Acton et al. 1992; Feldman et al. 1994). An asymmetry in the intensity profile across the loop-tops is also striking, with the intensity dropping quite sharply on the north sides of the knots, but more smoothly on the south sides. This is illustrated in Figure 8 where the intensity profile along an arc chosen to align with a flare loop from the 17:50:36 UT exposure is plotted. The asymmetry in the intensity distribution is clearly seen, with the intensity falling to its half-maximum value within 1 Mm on the north side of the apex, and within 2.2 Mm on the south side. Intensities along the displayed arc were derived through bilinear interpolation of the original image. We note that the exposure time for the 17:50:36 UT is not correct in the AIA data file, and so the commanded exposure time is used instead. This introduces an uncertainty of $\pm 7\%$ in the stated intensities (P. Boerner, 2014, private communication). IRIS spectra allow the properties of the loop-top brightenings to be compared with the loop legs.

Inspection of the $\lambda 1354.1$ profiles in the post-flare loops shows that they are very close to Gaussian in shape except for the blend with C I $\lambda 1354.29$, which is present in most spectra. For this reason we perform automatic Gaussian fits to the IRIS rasters, and extract intensity, velocity and line broadening parameters for the loop locations. At each spatial location we perform a three Gaussian fit to the wavelength window containing the Fe XXI line, with the additional two Gaussians used for C I $\lambda 1354.29$ and O I $\lambda 1355.60$. The EIS_AUTO_FIT suite of software (Young

Table 1. Properties of the IRIS flare ribbons.

Exposure	Ribbon	Ribbon appears	Fe XXI appears	Difference	Velocity (km s ⁻¹)	Position	Type
0	N1	R172	R173	1	-90	Offset	Compact
1	N1	R173	R173	0	-100	Ribbon	Compact
1	S1	R173	R174	1	-100	Ribbon	Diagonal-in
2	S1	R172	R174	2	-120	Offset	Diagonal-in
3	N2	R172	R173	1	0	Ribbon	Extended ^a
3	S1	R173	R174	1	-220 ^b	Ribbon	Diagonal-in
4	N2	R172	R173	1	-20	Ribbon	Extended ^a
4	S1	R173	R173	0	-120	Offset	Compact
5	N2	R172	R173	1	0	Ribbon	Extended ^a
5	S1	R173	R174	1	-160	Offset	Diagonal-out
6	N2	R171	R173	2	-120	Ribbon	Diagonal-in
6	S1	R172	R172	0	-20	Offset	Diagonal-out
7	N2	R172	R173	1	-10	Ribbon	Extended ^a
7	S1	R172	R174	2	-110	Offset	Compact

^aContaminated with flare loop emission.

^bVery broad and low intensity, so velocity uncertain.

2013) developed for the Hinode/EIS mission was modified to perform the fitting. This software allows parameter limits to be applied to the Gaussians to prevent spurious fits. For example, Fe XXI $\lambda 1354.1$ was restricted to full-width at half-maximum (FWHM) values between 0.35 and 1.41, while the much narrower O I $\lambda 1355.60$ line was restricted to FWHM values between 0.023 and 0.14 Å. In order to filter out the poor quality fits at the ribbon sites (due to blending with chromospheric lines), we considered only fits for which the integrated intensity was ≥ 50 DN s⁻¹, the absolute LOS velocity was ≤ 30 km s⁻¹ and the reduced χ^2 value for the fit was ≤ 1.5 .

From the Gaussian fits we can compare how parameters in the bright loop-tops compare with the loop legs. In Figure 9 we show an example from R179E6 (17:54:06 UT). This demonstrates that the LOS velocity is approximately zero at the loop-top ($Y=271\text{--}274''$), but increases to 7–8 km s⁻¹ in the southern loop legs ($Y=263\text{--}266''$), suggesting a draining of plasma to the loop footpoints. The line width shows no clear distinction between the loop-top and the legs, showing that the loop-top is not hotter than the legs, nor does it have an additional broadening component that may indicate turbulence. We note that Jakimiec et al. (1998) suggested a model for bright loop-tops whereby there are tangled magnetic field lines at the loop-top, and the motion of plasma on these field lines would result in non-thermal broadening to emission lines. The field is not tangled in the loop-legs in this model, which would lead to a lower non-thermal broadening in the emission lines. The IRIS spectra show that the loop-tops do not have an enhanced broadening compared to the loop-legs.

IRIS has higher spatial resolution than AIA and so allows the sizes of the loop-tops to be determined. There are a number of exposures where quite small features along the IRIS slit can be seen, and an example from R176E1 (17:49:34 UT) is shown in Figure 10a where there are three distinct structures, separated by about 1'' (725 km). Averaging the intensity over ± 20 km s⁻¹ either side of line center gives the intensity profile shown in Figure 10b, and Gaussian fits to the three structures give FWHM values of close to 1''. As this is significantly larger than the spatial resolution of the instrument, we consider the structures to be resolved by IRIS. Note that we consider the three structures to be the loop-tops of three distinct flare loops. Other exposures with similar examples of fine-scale structure include R176E2, R178E1 and R178E5.

Doschek et al. (1975) demonstrated that the Fe XXI line width decreased with time for one flare. In the present work we have spatially-resolved line width measurements and so we take the median value of the line width, W , from each of the rasters R174 to R179, and these are given in Table 2. The median was applied to between 614 and 1177 spatial pixels from these rasters. W can be interpreted as being entirely thermal in origin, in which case a temperature $T_{\text{th}} = 1.96 \times 10^{12} N W / \lambda$ K can be derived, where N is the mass number of the emitting element. The values of T_{th} are given in Table 2. This interpretation assumes an isothermal plasma, and the results imply cooling as the flare decays. An alternative interpretation comes from assuming that $\lambda 1354.1$ is formed at its temperature of maximum emission ($\log T/\text{K} = 7.06$), in which case line broadening beyond the thermal width at this temperature corresponds to non-thermal plasma

motions. The non-thermal motions are represented by the velocity ξ , given by

$$4 \ln 2 \left(\frac{\lambda}{c} \right)^2 \xi^2 = W^2 - W_{\text{th}}^2, \quad (3)$$

where c is the speed of light and W_{th} the width at $\log T/\text{K} = 7.06$. Table 2 gives the values of ξ assuming this interpretation, and they show non-thermal motions decreasing from 43 to 26 km s^{-1} over a six minute period. We note that Doschek et al. (1975) found peak non-thermal motions of 60 km s^{-1} , falling to 5 km s^{-1} about 14 minutes later. In Figure 11 we consider the distribution of widths across two rasters separated by 5 minutes. A cumulative distribution function is used and the total number of spatial pixels was 841 and 1177 for R175 and R179, respectively. The distributions demonstrate that, on the whole, the widths decreased by 0.02 \AA over this time, but also that there are more large widths in the earlier raster: 8% of spatial pixels have widths $\geq 0.55 \text{\AA}$ for R175, compared to less than 2% for R179. If the measured widths are interpreted purely as thermal widths, then they imply mostly $\log T \leq 7.35$ for R175 and $\log T \leq 7.25$ for R179. We also note there are very few pixels for which the width is below the thermal width at $\log T = 7.06$, the temperature of maximum emission of $\lambda 1354.1$, which gives confidence that this value is accurate.

Away from the ribbons, the Doppler shifts of $\lambda 1354.1$ are modest and in fact the IRIS data can be used to estimate a new reference wavelength of 1354.106 \AA for the line (Appendix B). Figure 12 shows intensity, velocity and line width maps derived from IRIS raster R179, compared to a co-temporal A131 image. Note that a pixel size of $2''$ in the X-direction is used for displaying the IRIS images but in reality each column represents only a region $0.33''$ in the X-direction. The velocity map is derived assuming the rest wavelength of 1354.106 \AA for the Fe XXI line (Appendix B). If the value of 1354.064 \AA from Feldman et al. (2000) is used, then all velocities would be increased by 9 km s^{-1} , making the loop arcade almost entirely red-shifted. Figure 12c shows that the region around spatial location (516,260) is red-shifted by around 10–20 km s^{-1} and this pattern persists throughout rasters R174 to R179. The northern loop legs generally show a weak blue-shift of a few km s^{-1} , but with an uncertainty of $\pm 5 \text{ km s}^{-1}$ in the rest wavelength of the Fe XXI line (Appendix B) this is not significant.

6. Conclusions

In this work we have presented observations of the Fe XXI $\lambda 1354.1$ emission line obtained by IRIS during the 2014 March 29 X1 flare. The high spatial resolution and sensitivity of the IRIS instrument allows high temperature ($\approx 10 \text{ MK}$) plasma to be studied on much smaller spatial scales than previously possible. This has enabled fine structure in the post-flare loop arcade and the flare ribbons to be studied. We distinguish the Fe XXI emission at the flare ribbons from that in the post-flare loop arcade, and we consider that the ribbons represent the footpoints of the post-flare loops. The results for the ribbons are given below.

1. The Fe XXI $\lambda 1354.1$ line generally appears at the flare ribbon site about 75 seconds after the

flare ribbon appears at chromospheric temperatures.

2. The $\lambda 1354.1$ emission when it first appears at the ribbons is mostly compact with a spatial extent $< 2''$.
3. The line is blue-shifted, implying plasma flowing up into the corona, with line-of-sight speeds of $100\text{--}200 \text{ km s}^{-1}$. Examples of both decreasing and increasing speed with distance from the ribbons were found.
4. Blue-shifted $\lambda 1354.1$ at the ribbons was present until the end of the IRIS observing sequence at 17:54 UT, 6 minutes after the flare peak.
5. Studies of $\lambda 1354.1$ at the ribbons are compromised by a number of chromospheric emission lines that are found between 1352.5 and 1354.0 \AA at the ribbon locations and are comparable in strength to $\lambda 1354.1$.

The post-flare loop $\lambda 1354.1$ emission began to appear during the impulsive phase of the flare and developed into an extended loop arcade with bright loop-tops. The key results are listed below.

1. The AIA 131 \AA filter images, which are dominated by $\text{Fe XXI } \lambda 128.7$, show that the bright loop-tops have an asymmetric intensity distribution, being more extended on the south-side of the loops.
2. The loop-tops are resolved by IRIS and have sizes of $\geq 1''$.
3. IRIS Doppler maps formed from $\lambda 1354.1$ show small Doppler shifts in the loop arcade, corresponding to velocities of typically $\leq 10 \text{ km s}^{-1}$.
4. Velocities at the loop-tops are close to rest, and the $\lambda 1354.1$ width is not significantly enhanced compared to the loop legs.
5. On average there is a slow decrease in the width of the $\lambda 1354.1$ emission line of about 0.02 \AA over 5 minutes, and there is a greater dispersion of widths near the peak of the flare.
6. Assuming the loop arcade emission is, on average, at rest then a new rest wavelength of $1354.106 \pm 0.023 \text{ \AA}$ is derived for the Fe XXI line.

The IRIS instrument has significant flexibility in terms of observation programs and so we highlight here some of the advantages and disadvantages of the observing sequence used for the March 29 flare. Firstly, the eight second exposure time is ideal for studying $\text{Fe XXI } \lambda 1354.1$ as it yields sufficient signal to study the weak profiles seen at the ribbons, but also the intensities in the post-flare loops do not reach sufficiently high levels that saturation sets in. In particular we note that if the exposure times had been reduced by automatic exposure control then this would have made studying the ribbon emission difficult.

The raster type used for the observation was a “coarse 8-step raster”, which had 2'' jumps between slit positions. This enabled a fairly large spatial region to be covered rapidly in X, with the downside of poor sampling. As the IRIS slit did not lie directly along the axes of the post-flare loops, the jumps in X-position generally meant that only small sections of the loops could be observed spectroscopically. In particular the footpoint emission shown in Figure 5 generally terminated abruptly in Y a short distance from the ribbon. A “dense raster”, i.e., step sizes equal to the slit width would have enabled us to check if the variation of footpoint emission with height along the loops could be tracked in the X-direction.

Finally, the wavelength window used for $\lambda 1354.1$ is not sufficiently large, with at least one profile (Figure 4c) partially extending beyond the window edge at -350 km s^{-1} . Presently there are five options offered to observers for line-lists, and the “flare line-list” was used for this observation. Extending the 1354 \AA window to at least -500 km s^{-1} from line center is recommended. Also extending the window by around 50 km s^{-1} on the long wavelength side would also be beneficial as O I $\lambda 1355.60$ (a line needed for wavelength calibration) is partly out of the window at some locations.

P.R.Y. acknowledges funding from NASA grant NNX13AE06G and National Science Foundation grant AGS-1159353. H.T. is supported by contracts 8100002705 and SP02H1701R from LMSAL to SAO. IRIS is a NASA small explorer mission developed and operated by LMSAL with mission operations executed at NASA Ames Research center and major contributions to downlink communications funded by the Norwegian Space Center (NSC, Norway) through an ESA PRODEX contract. SDO is a mission for NASA’s Living With a Star program, and data are provided courtesy of NASA/SDO and the AIA and HMI science teams.

Facilities: IRIS, SDO(AIA), GOES.

A. Blending lines near Fe XII $\lambda 1354.1$

In flare spectra, particularly near the ribbons, a number of emission lines become prominent that are not normally measurable in the IRIS spectra. Some of these lines compromise measurements of Fe XXI $\lambda 1354.1$ and so we discuss these lines here. We note that the large width of $\lambda 1354.1$ compared to the cool blending lines means that it is relatively easy to identify $\lambda 1354.1$, but the lines affect the measurement of the line parameters (intensity, centroid and width). As discussed in Sect. 4, the ribbons typically appear in chromospheric lines one raster earlier than they do in $\lambda 1354.1$, so in Figure 13 we show examples of ribbon spectra without the $\lambda 1354.1$ line in order to better display the blending lines. These spectra can be compared with Figure 4 which shows four examples where $\lambda 1354.1$ is present.

The spectrum in Figure 13a is the most common type of ribbon spectrum, with two lines of Si II and one of Fe II becoming comparable in intensity to C I $\lambda 1354.29$. The two Si II lines often

show interesting dynamics at the flare ribbons, with broad long-wavelength wings extending up to 150 km s^{-1} . The broad wings can be confused with Fe XXI emission, but the presence of two Si II lines enables the Si II components to be easily identified.

Figure 13b shows a spectrum about $1''$ from a ribbon where a pair of very close lines are found at 1353.32 and 1353.39 \AA . By comparing the intensity distribution along the slit, these lines show similar behavior to a pair of lines at 1333.48 and 1333.80 \AA that are known to be H_2 lines fluoresced by Si IV (Bartoe et al. 1979). Another possibility is that they are CO lines, although they are not listed by Jordan et al. (1979).

An unusual spectrum is seen in a few of the flare exposures and an example is shown in Figure 13c. Two lines at 1353.55 and 1354.19 \AA are particularly prominent and are striking because of their very narrow widths of $\approx 0.045 \text{ \AA}$. The lines have a very different intensity distribution along the slit compared to the atomic lines or H_2 and there are many similar lines in the spectrum including a distinctive group of 5–6 lines between 1402.0 and 1402.5 \AA , on the short wavelength side of Si IV $\lambda 1402.77$.

B. The rest wavelength of Fe XXI $\lambda 1354.1$

For creating velocity maps from Fe XXI $\lambda 1354.1$ it is necessary to set an absolute wavelength scale. For this we use O I $\lambda 1355.60$ which is a narrow chromospheric line that demonstrates only small Doppler shifts in rasters. The reference wavelength for this line is 1355.5977 \AA , which is a calculated value with an accuracy estimated at 0.5 m\AA (Eriksson & Isberg 1968). As described in Sect. 5 we fit three Gaussians to the wavelength window containing Fe XXI $\lambda 1354.1$, one of which represents the O I line.

We used rasters R177–179 to determine the Fe XXI wavelength as these show strong emission from the post-flare loops, and the line is mostly close to the rest wavelength. We restrict analysis to those spatial pixels for which the $\lambda 1354.1$ line width is between 0.42 and 0.55 \AA , i.e., close to the thermal width of 0.43 \AA , the integrated intensity is $\geq 50 \text{ DN}$, and the reduced χ^2 value for the fit is ≤ 1.5 . These restrictions remove pixels for which the line shows unusual dynamics, is weak, or has a poor fit. For these spatial pixels we take the set of O I centroids, measured through a Gaussian fit, and compute the mean and standard deviations. These values are shown in Table 3. Similarly the mean and standard deviation of the Fe XXI wavelengths are computed. We correct the derived Fe XXI wavelength by the difference between the derived and reference O I wavelengths, giving the rest Fe XXI wavelengths shown in Table 3. The uncertainty has been obtained by adding in quadrature the standard deviations of the measured Fe XXI and O I wavelengths, and the uncertainty in the O I reference wavelength. Combining these results gives a final rest wavelength of $1354.106 \pm 0.023 \text{ \AA}$, which we adopt in the present work.

We note that there is a significant discrepancy with the value of $1354.064 \pm 0.020 \text{ \AA}$ from Feldman et al. (2000). If this value is correct, then it implies that the post-flare loops in the

present observation are, on average, red-shifted by 9 km s^{-1} .

REFERENCES

- Acton, L. W., et al. 1992, PASJ, 44, L71
- Ayres, T. R., Brown, A., Harper, G. M., Osten, R. A., Linsky, J. L., Wood, B. E., & Redfield, S. 2003, ApJ, 583, 963
- Bartoe, J.-D. F., Brueckner, G. E., Nicolas, K. R., Sandlin, G. D., Vanhoosier, M. E., & Jordan, C. 1979, MNRAS, 187, 463
- Benz, A. O. 2008, Living Reviews in Solar Physics, 5
- Cheng, C.-C., Feldman, U., & Doschek, G. A. 1979, ApJ, 233, 736
- De Pontieu, B., et al. 2014, Sol. Phys., 289, 2733
- Dere, K. P., Landi, E., Mason, H. E., Monsignori Fossi, B. C., & Young, P. R. 1997, A&AS, 125, 149
- Doschek, G. A., Dere, K. P., Sandlin, G. D., Vanhoosier, M. E., Brueckner, G. E., Purcell, J. D., Tousey, R., & Feldman, U. 1975, ApJ, 196, L83
- Doyle, J. G., & Phillips, K. J. H. 1992, A&A, 257, 773
- Eriksson, K. B. S., & Isberg, H. B. S. 1968, Ark. Fys., 37, 221
- Feldman, U., Curdt, W., Landi, E., & Wilhelm, K. 2000, ApJ, 544, 508
- Feldman, U., Seely, J. F., Doschek, G. A., Strong, K. T., Acton, L. W., Uchida, Y., & Tsuneta, S. 1994, ApJ, 424, 444
- Handy, B. N., et al. 1999, Sol. Phys., 187, 229
- Innes, D. E., Curdt, W., Schwenn, R., Solanki, S., Stenborg, G., & McKenzie, D. E. 2001, ApJ, 549, L249
- Innes, D. E., McKenzie, D. E., & Wang, T. 2003a, Sol. Phys., 217, 267
- Innes, D. E., McKenzie, D. E., & Wang, T. 2003b, Sol. Phys., 217, 247
- Jakimiec, J., Tomczak, M., Falewicz, R., Phillips, K. J. H., & Fludra, A. 1998, A&A, 334, 1112
- Jordan, C., Bartoe, J.-D. F., Brueckner, G. E., Nicolas, K. R., Sandlin, G. D., & Vanhoosier, M. E. 1979, MNRAS, 187, 473

Table 2. Average properties derived from Fe xxI λ 1354.1 line widths.

Time ^a	Raster	W (\AA)	ξ (km s^{-1})	$\log(T_{\text{th}}/\text{K})$
17:47:27	R174	0.543	42.8	7.25
17:48:42	R175	0.493	30.0	7.16
17:49:57	R176	0.489	28.9	7.16
17:51:12	R177	0.491	29.6	7.16
17:52:26	R178	0.482	26.9	7.14
17:53:41	R179	0.481	26.3	7.14

^aThe midpoint time of the raster.

Table 3. Measured wavelengths for O I and Fe xxI.

Raster	O I	Fe xxI
R177	1355.6204 ± 0.0090	1354.106 ± 0.023
R178	1355.6205 ± 0.0080	1354.106 ± 0.022
R179	1355.6211 ± 0.0078	1354.107 ± 0.023

- Kliem, B., Dammasch, I. E., Curdt, W., & Wilhelm, K. 2002, *ApJ*, 568, L61
- Landi, E., Feldman, U., Innes, D. E., & Curdt, W. 2003, *ApJ*, 582, 506
- Landi, E., Young, P. R., Dere, K. P., Del Zanna, G., & Mason, H. E. 2013, *ApJ*, 763, 86
- Lemen, J. R., et al. 2012, *Sol. Phys.*, 275, 17
- Maran, S. P., et al. 1994, *ApJ*, 421, 800
- Mason, H. E., Shine, R. A., Gurman, J. B., & Harrison, R. A. 1986, *ApJ*, 309, 435
- Milligan, R. O., Gallagher, P. T., Mathioudakis, M., Bloomfield, D. S., Keenan, F. P., & Schwartz, R. A. 2006, *ApJ*, 638, L117
- Sandlin, G. D., Brueckner, G. E., & Tousey, R. 1977, *ApJ*, 214, 898
- Teriaca, L., Falchi, A., Cauzzi, G., Falciani, R., Smaldone, L. A., & Andretta, V. 2003, *ApJ*, 588, 596
- Teriaca, L., Falchi, A., Falciani, R., Cauzzi, G., & Maltagliati, L. 2006, *A&A*, 455, 1123
- Wang, T. J., Solanki, S. K., Curdt, W., Innes, D. E., Dammasch, I. E., & Kliem, B. 2003a, *A&A*, 406, 1105
- Wang, T. J., Solanki, S. K., Innes, D. E., Curdt, W., & Marsch, E. 2003b, *A&A*, 402, L17
- Watanabe, H., Vissers, G., Kitai, R., Rouppe van der Voort, L., & Rutten, R. J. 2011, *ApJ*, 736, 71
- Xu, Y., Cao, W., Jing, J., & Wang, H. 2012, *ApJ*, 750, L7
- Young, P. R. 2013, EIS Software Note No. 16, ver. 2.5
- Young, P. R., Doschek, G. A., Warren, H. P., & Hara, H. 2013, *ApJ*, 766, 127

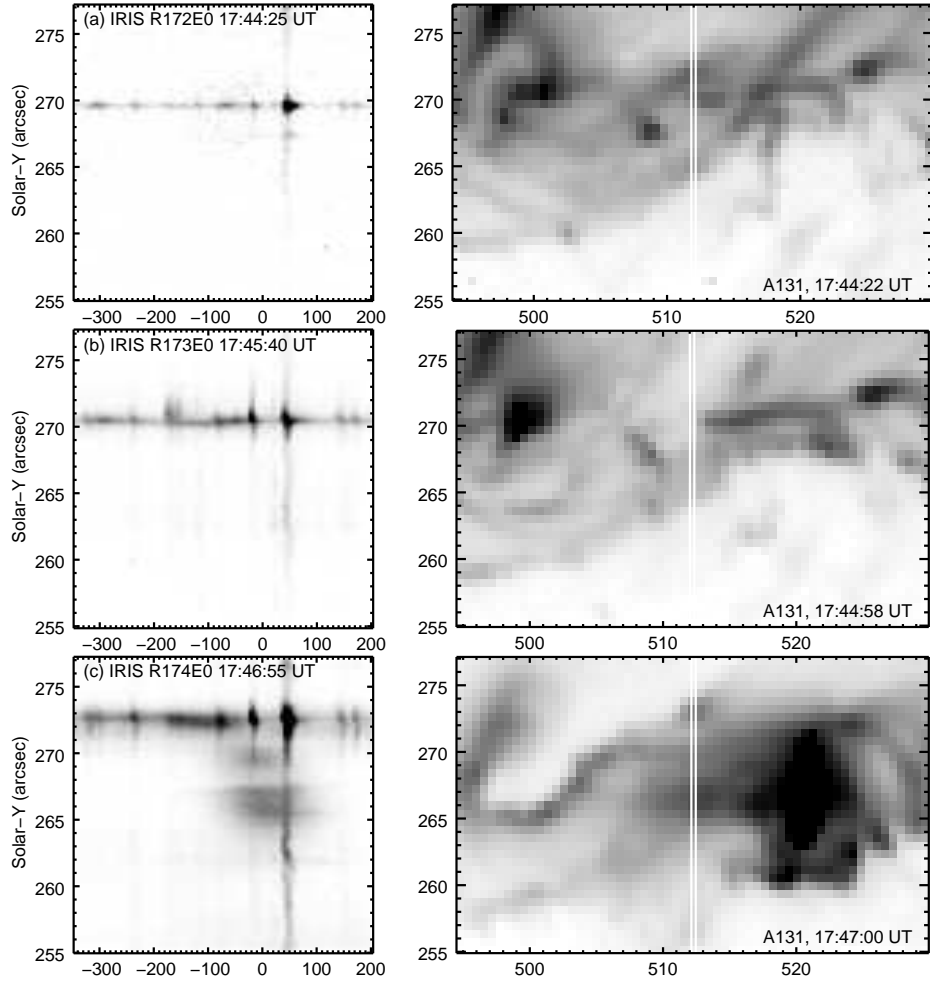


Fig. 3.— Sequence of three images showing the development of the Fe XXI $\lambda 1354.1$ line at a location on the N1 flare ribbon. The left column shows IRIS detector images with a reverse-linear intensity scaling applied. A saturation has been applied to better reveal the weak Fe XXI line. The right column shows A131 images close in time to the IRIS images. An inverse-square-root intensity scaling has been applied. The parallel white lines indicate the location of the IRIS slit.

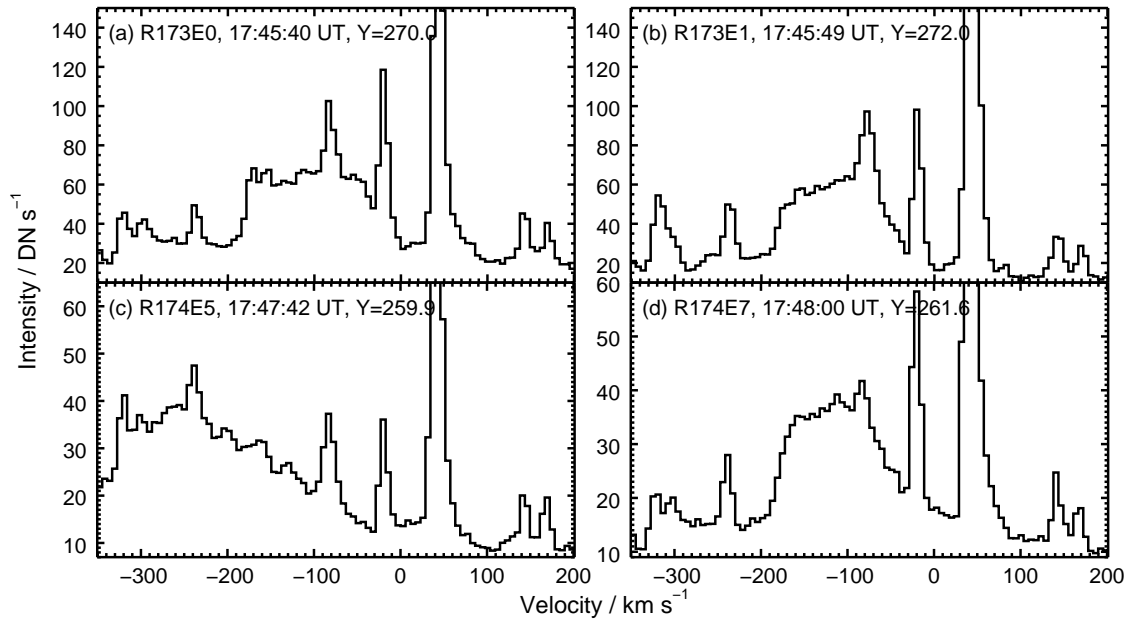


Fig. 4.— Four examples of Fe XXI $\lambda 1354.1$ line profiles from locations at or close to the flare ribbons. The profiles have been obtained for individual solar-Y pixels, and the Y-values are indicated on the plots.

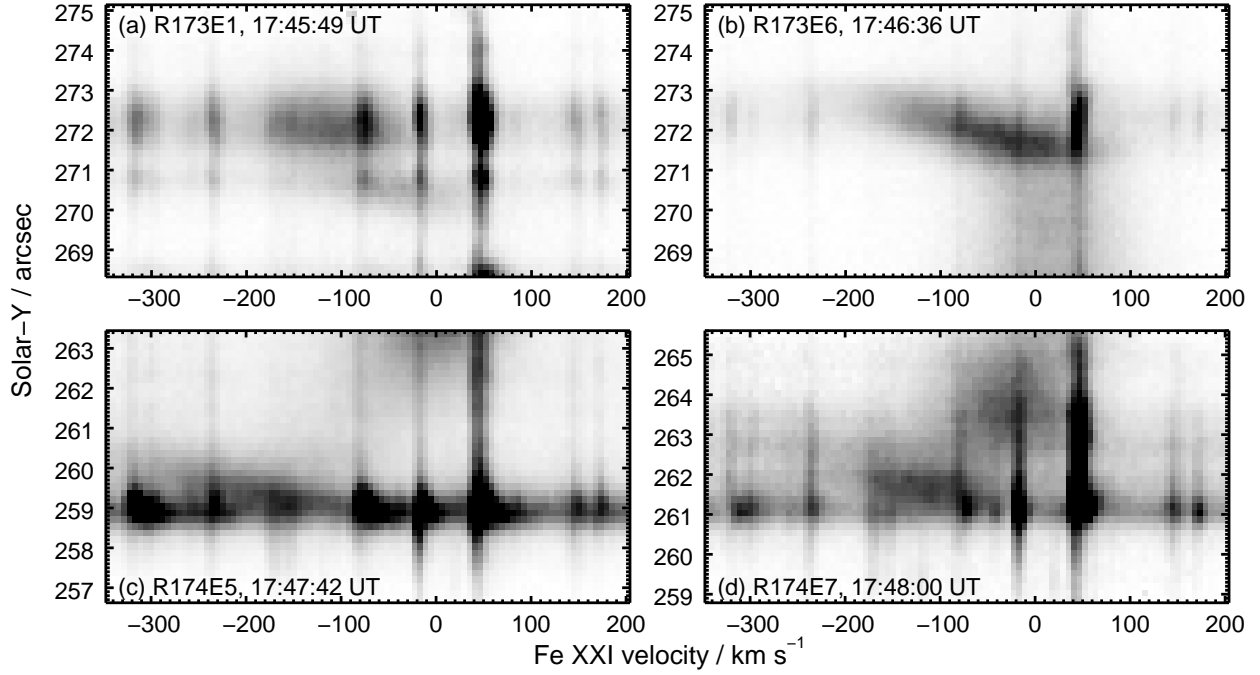


Fig. 5.— Four IRIS detector images showing different examples of Fe XXI emission at the flare ribbon sites. An inverse-linear intensity scaling has been applied, and the images have been saturated to better reveal the Fe XXI line.

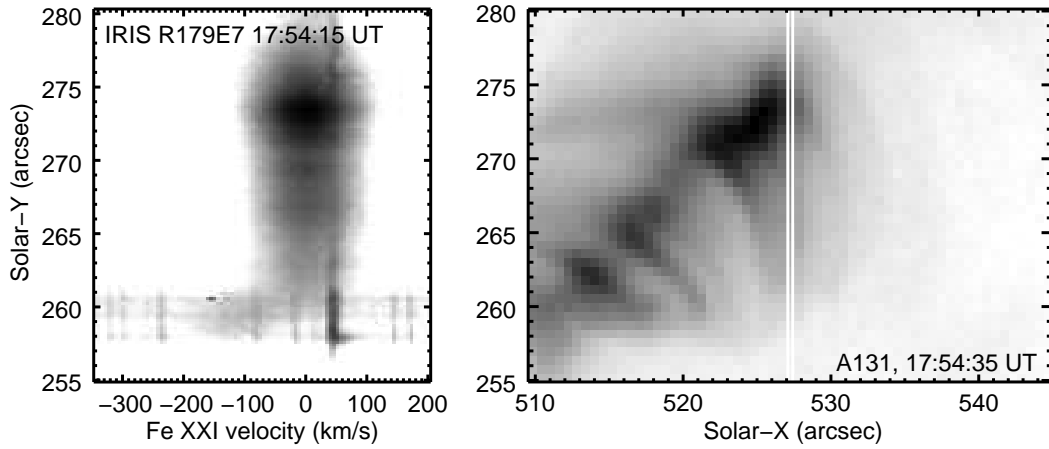


Fig. 6.— The left panel shows an IRIS detector image from 17:54:15 UT, plotted with a reverse-logarithmic intensity scaling. The right panel shows an A131 image, plotted with a reverse-square-root intensity scaling. Parallel white lines show the location of the IRIS slit.

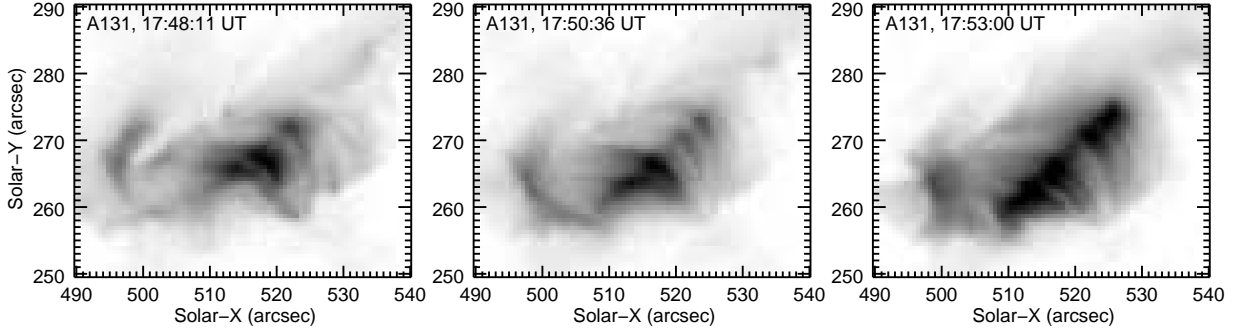


Fig. 7.— Three A131 images showing the post-flare loop arcade at different times. A cubed-root scaling has been applied and the color table reversed. The brightest areas (black) are saturated in each of the frames.

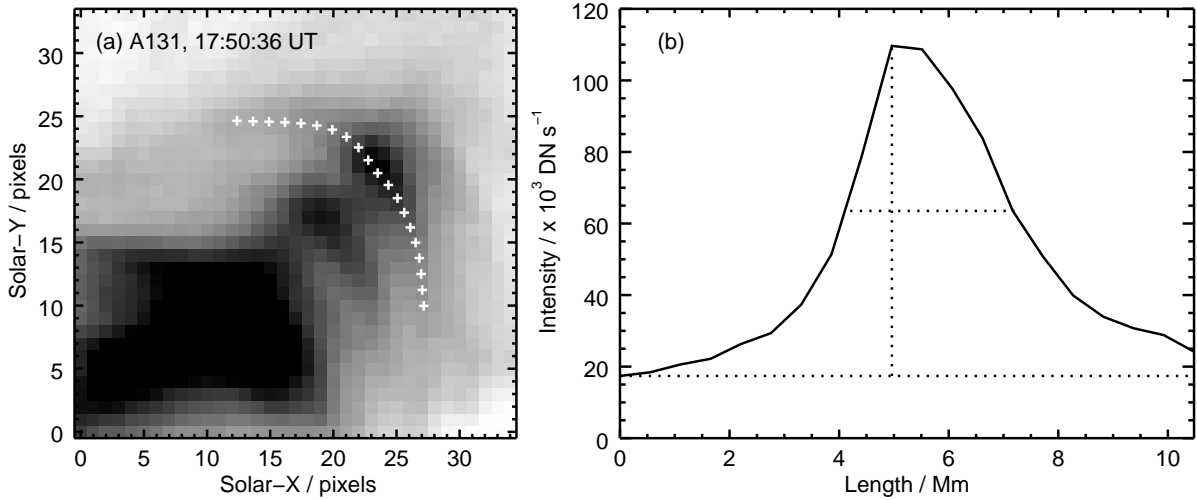


Fig. 8.— Panel (a) shows an A131 image from 17:50:36 UT. A square-root intensity scaling has been applied and the color table reversed. Interpolated intensities for the spatial locations identified by crosses on this image are plotted in Panel (b). Dotted lines show the locations of the maximum, minimum and half-maximum intensities.

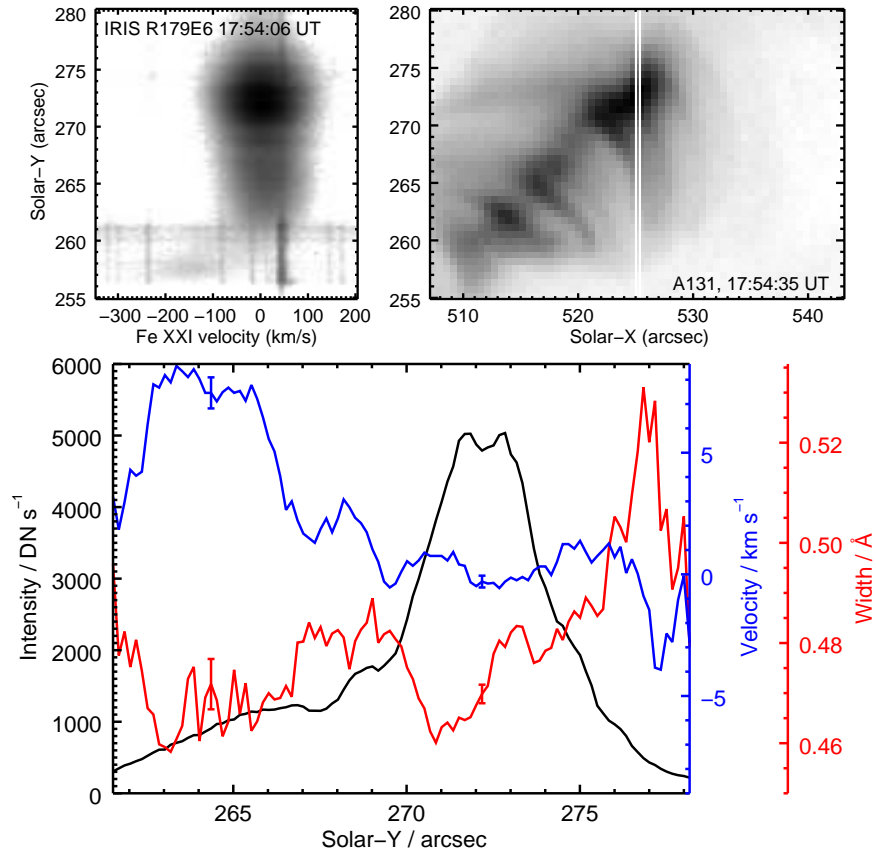


Fig. 9.— Fe XII $\lambda 1354.1$ Gaussian fit parameters as a function of solar-Y position from R179E6 (17:56:06 UT). The black line shows the line intensity (DN s^{-1}), the blue line shows LOS velocity (km s^{-1}), and the red line shows line width (\AA). Fitting uncertainties at example locations are indicated.

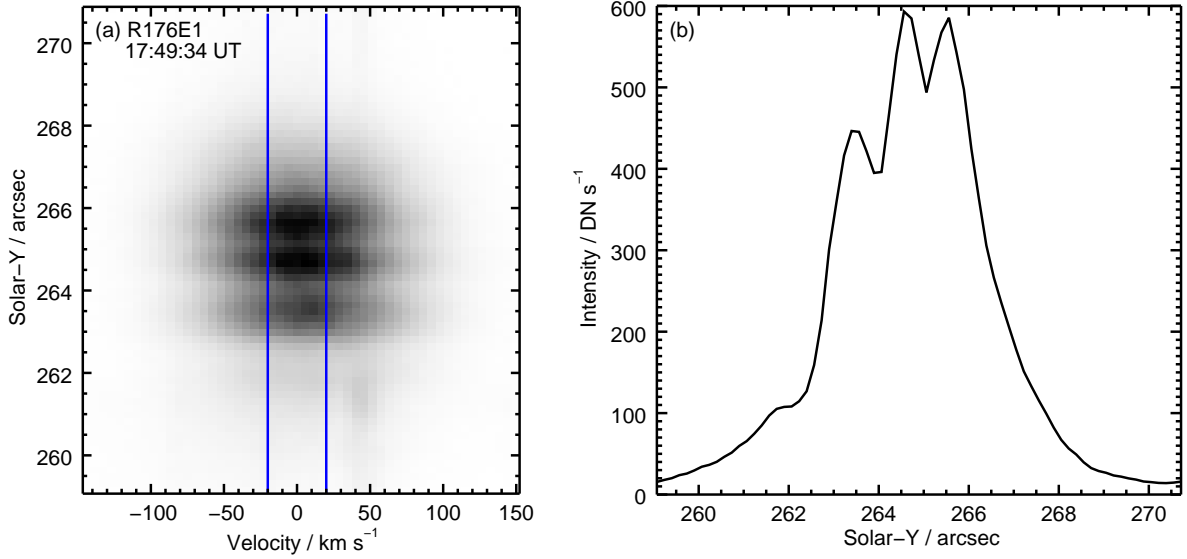


Fig. 10.— Panel (a) shows an IRIS detector image from 17:49:34 UT, showing strong Fe XXI $\lambda 1354.1$ emission. Averaging the intensity over $\pm 20 \text{ km s}^{-1}$ from line center gives the intensity profile with solar-Y position shown in panel (b).

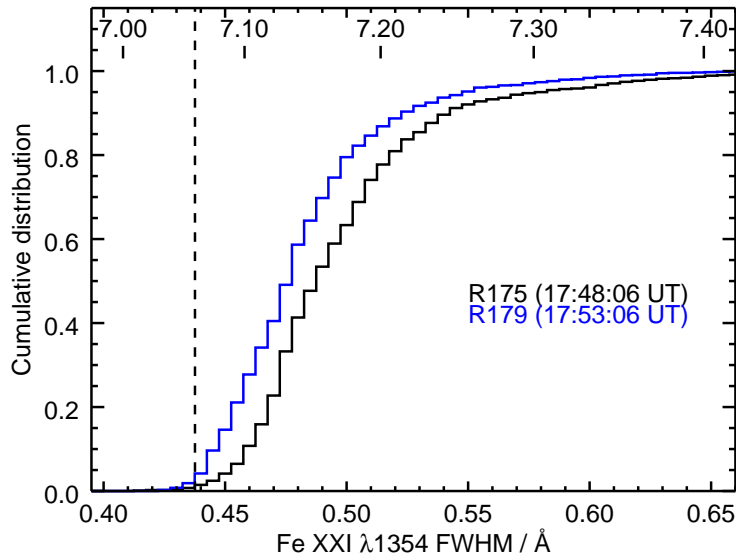


Fig. 11.— Cumulative distributions of Fe XXI $\lambda 1354.1$ line widths from rasters R175 and R179. Logarithmic temperatures corresponding to the widths, assuming they are entirely thermal in origin, are indicated. The vertical dashed line indicates the thermal width at the peak formation temperature ($\log T = 7.06$) of Fe XXI $\lambda 1354.1$.

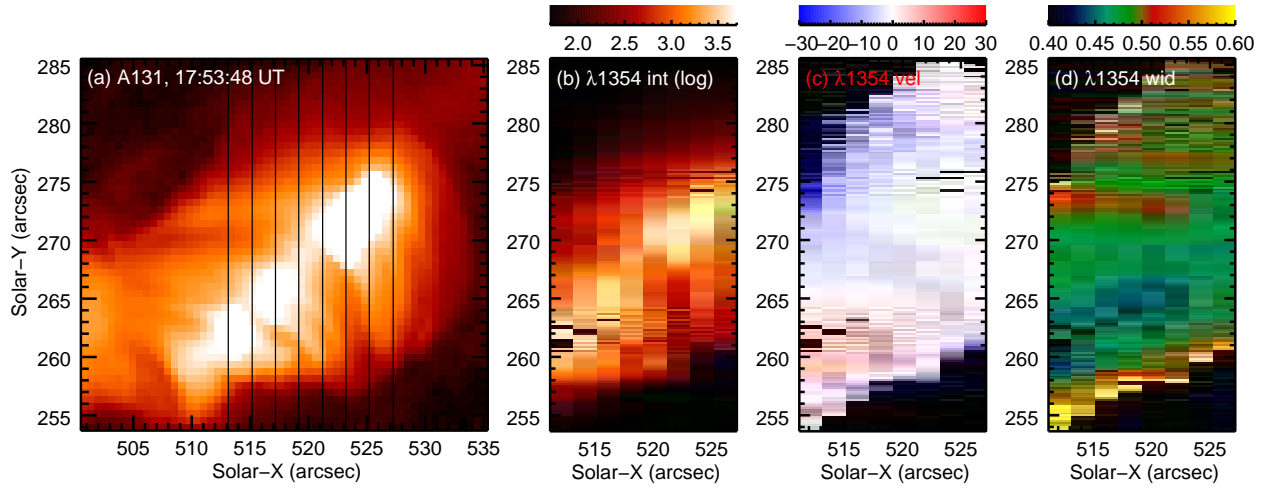


Fig. 12.— Panel (a) shows the A131 image from 17:53:48 UT with a logarithmic intensity scaling. The brightest parts of the image are saturated, and the eight vertical lines show the locations of the IRIS slit for raster R179. Panels (b), (c) and (d) show the Fe XXI $\lambda 1354.1$ intensity (logarithm), velocity and width, in units of DN s^{-1} , km s^{-1} , and \AA , respectively.

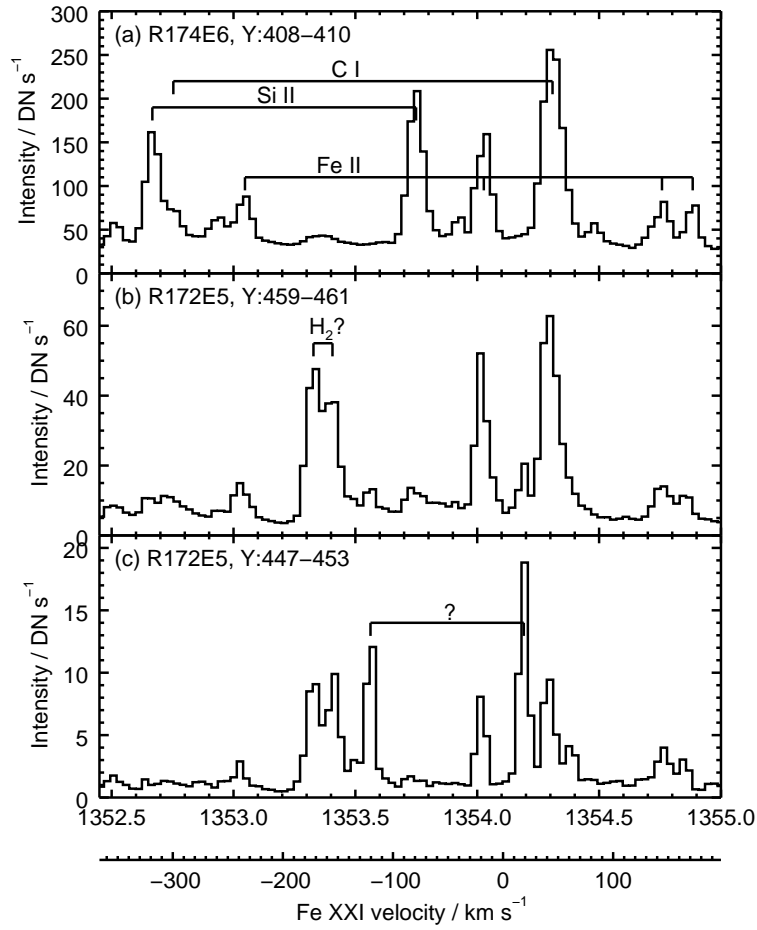


Fig. 13.— Three examples of IRIS spectra at or in the vicinity of flare ribbons. The Y-pixel ranges over which the spectra are averaged are indicated.